

TES INSTRUMENT AND THERMAL STRUCTURE OBSERVATIONS

M. D. Smith¹, B. J. Conrath², J. C. Pearl¹, and P. R. Christensen³,

¹NASA Goddard Space Flight Center, Greenbelt, MD 20771 USA (Michael.D.Smith.1@gssc.nasa.gov), ²Cornell University, Ithaca, NY 14853 USA, ³Arizona State University, Tempe, AZ 85287 USA.

Introduction: The Mars Global Surveyor (MGS) began mapping operations from Mars orbit on March 1, 1999 ($L_s=104^\circ$), and has now provided nearly continuous monitoring of conditions in the Martian atmosphere for almost two full Martian years. Infrared spectra taken by the Thermal Emission Spectrometer (TES) on-board MGS are very well suited for monitoring Martian atmospheric conditions. The atmospheric thermal structure, dust and water ice aerosol optical depth, and water vapor column abundance can all be retrieved from each TES spectrum. This allows the latitudinal, longitudinal, and seasonal dependences of these quantities to be examined in unprecedented detail. TES builds on earlier spacecraft observations of Mars by Mariner 9 and the Viking orbiters by providing increased spatial and temporal resolution and more complete spatial and seasonal coverage. Comparison of Mariner 9, Viking, and TES results allows interannual variability to be evaluated. Previous reports of results relating to the Mars atmosphere from TES have used data taken during the aerobraking and science phasing (pre-mapping) phases of the MGS mission [Christensen *et al.* 1998; Conrath *et al.*, 2000; Smith *et al.*, 2000a, b; Clancy *et al.*, 2000; Pearl *et al.*, 2001; Bandfield *et al.*, 2000], or during the first portion of MGS mapping [Smith *et al.*, 2001, 2002; Smith 2002].

TES Data Characteristics: The Thermal Emission Spectrometer (TES) is a thermal infrared interferometer/spectrometer with additional broadband visible and thermal channels [Christensen *et al.*, 1992; 2001]. Six detectors in a three-by-two array simultaneously take spectra covering the spectral range from 200 to 1600 cm^{-1} (6-50 μm), with a selectable spectral resolution of either 6.25 or 12.5 cm^{-1} . A pointing mirror allows TES to observe from nadir to above both the forward and aft limbs, where the atmosphere is observed without direct contribution from the surface. Each pixel subtends a 8.3-mrad field of view.

MGS is in a near-polar, sun-synchronous (local time \sim 0200 and 1400 hours) orbit with the ascending node at 1400 hours. TES data have a spatial resolution of 3 km across-track and 10-20 km along track (because of smear caused by spacecraft motion). The MGS mapping orbit gives one narrow strip of observations running roughly north-south. One day of data gives two sets of twelve such strips spaced roughly 29° apart in longitude, with one set taken near a local time of 0200 hours and the other near 1400 hours. For this work, we use only the daytime (1400 hours) data. We do not use nighttime data because 1) they have lower

signal-to-noise, 2) the atmospheric temperature profiles retrieved from nighttime TES data potentially have relatively large uncertainties near the surface due to the near-surface nighttime inversion in the boundary layer, and 3) the large mixture of surface temperature observed over a TES pixel caused by the differences in thermal inertia at scales smaller than a TES pixel.

The primary mode of TES data acquisition is with the field-of-view pointed toward nadir. However, every 10° - 20° of latitude around the orbit, a sequence of limb-geometry observations is taken with the field-of-view pointed to observe the atmosphere above the limb. Because the nadir-geometry observations are far more numerous, they are generally used for mapping the spatial distribution of aerosol optical depth. Retrieval of the atmospheric thermal structure uses a combination of observations from nadir-geometry spectra giving information about the lowest 30 km above the surface and limb-geometry spectra giving information from roughly 30-65 km.

Retrieval Methods: A detailed description of the retrieval algorithms for atmospheric temperatures and aerosol opacities is given by [Smith *et al.*, 2000a] (dust optical depth), [Pearl *et al.*, 2001] (water-ice optical depth), [Conrath *et al.*, 2000] (atmospheric temperatures), and [Smith 2002] (water vapor column abundance). Here we describe the retrievals in outline. The retrievals of atmospheric temperature and aerosol opacity are performed sequentially. Atmospheric temperatures are retrieved using a constrained linear inversion of radiance in the $15\text{-}\mu\text{m}$ CO_2 band. In this retrieval we have accounted for aerosol opacity to first order by using an effective surface temperature calculated by taking the brightness temperatures in narrow spectral intervals on either side of the CO_2 band and averaging them. The spectral intervals are 508-529 and $814\text{-}825\text{ cm}^{-1}$. Temperatures from the surface to \sim 0.1 mbar (35 km) are obtained from nadir-geometry spectra with a typical vertical resolution of about one scale height (10 km). Temperature profiles can be extracted from 1.0 to 0.01 mbar (65 km), where limb-geometry spectra are available (typically every 10° in latitude). Complete temperature profiles to 0.01 mbar are obtained by splicing the two temperature profiles through averaging in the 0.1- to 1.0-mbar range. Individual temperature profiles have a typical uncertainty of \sim 2 K except in the lowest scale height above the ground, where the uncertainty is somewhat larger.

Aerosol opacities are retrieved after the temperature retrieval is performed. To do so, we first compute the equivalent column-integrated opacity of a pure absorber

as a function of wave number. Then, we estimate the contribution of dust and water ice to the total opacity by performing a least squares fit of predetermined spectral shapes (opacity as a function of wave number) for dust, water ice, and the effect of a non-unit emissivity surface to the observed opacity spectrum. The predetermined spectral shapes for dust and water ice are determined from TES data and are described by *Smith et al.* [2000b] and *Bandfield et al.* [2000]. The retrieval of aerosol opacities is restricted to those spectra with a surface temperature >220 K. This constraint ensures that there is sufficient thermal contrast between the surface and the atmosphere for an accurate retrieval.

The retrieval of aerosol opacity uses two major simplifying assumptions. We assume that (1) the aerosol is well-mixed with the CO_2 gas and that (2) the aerosols are non-scattering. The first assumption has been found to be good for dust in Viking [*Pollack et al.*, 1977], Pathfinder [*Smith et al.*, 1997], and TES data [*Smith et al.*, 2000a]. However, water ice is often present in stratified clouds [*Pearl et al.*, 2001]. Numerical experiments show that for typical daytime conditions opacities can be overestimated by 20-50%. This uncertainty does not affect the identification of water-ice clouds or our statistics on their occurrence with season or location. However, until we have a better understanding from limb-geometry observations about the heights and temperatures at which water-ice clouds form, we do not feel we should attempt to correct for this bias.

The second assumption, that the aerosols are non-scattering, has been shown to be good to 10-20% when aerosol opacities are not too large [*Smith et al.*, 2000a]. During the dustiest times (dust storms), when dust optical depth reaches unity or higher, scattering becomes more important, and the optical depth estimates presented here become more of an indicator of relative dust optical depth than an absolute measure of the amount of dust in the atmosphere.

Overview of TES Atmospheric Observations:

The results presented below were derived using data covering nearly two full Martian years from $L_s=104^\circ$ (March 1, 1999) to $L_s=71^\circ$ (September 21, 2002). In Figure 1 we show maps of dust optical depth (1075 cm^{-1}), the atmospheric temperature at 0.5 mbar, water-ice optical depth (825 cm^{-1}), and water vapor column abundance. Zonal means of dayside (1400 hours) nadir-viewing data are presented. The retrieval of aerosol optical depth and water vapor abundance is restricted to those spectra with a surface temperature >220 K to ensure adequate thermal contrast between the surface and the atmosphere. Because dust optical depth is usually nearly well-mixed with CO_2 , it has been scaled to a 6.1-mbar equivalent pressure surface to remove the effect of topography. Water-ice optical depth and water vapor abundance are not as closely well-mixed as dust and so are not scaled. Estimated uncertainties in Fig. 1 are 2 K for temperatures, 0.02 for aerosol optical

depth, and 3 μm for water vapor abundance.

The difference between the perihelion and aphelion seasons (currently $L_s=251^\circ$ and 71° , respectively), and the interrelations between the four quantities shown in Figure 1 are striking. Dust and water-ice aerosol and water vapor abundance will be discussed further in an accompanying abstract. Here we focus on the 0.5-mbar temperatures.

Apparent in the second panel of Figure 1 are two superimposed trends. First is a planet-wide warming and cooling of the middle atmosphere in response to the change in solar insolation between aphelion and perihelion. Second are several episodes of heating (notable ones are at $L_s=225^\circ$ and 260° during the first year and at $L_s=185^\circ$ during the second year) associated with dust storms. The largest dust storm ($L_s=185^\circ$ during the second year) caused atmospheric temperatures to rise by more than 40 K over a large portion of the globe [*Smith et al.* 2002]. Heating associated with dust storms is caused both by direct solar heating from an increased amount of suspended dust, as well as dynamically by adiabatic heating in the descending branch of an enhanced Hadley circulation. Both mechanisms respond to changes in dust loading quickly (within a few sols).

Temperature Cross-Sections: Figure 2 shows latitude-pressure cross-sections of atmospheric temperature for each of the four seasons, $L_s=0^\circ, 90^\circ, 180^\circ, 270^\circ$. Data from both nadir- and limb-geometry observations have been combined to form these cross-sections.

Temperatures are generally found to depart significantly from radiative equilibrium, indicating strong modifications of the thermal structure by dynamical processes. Under solstice conditions, the temperatures at all levels are found to increase monotonically toward the summer pole with a strong polar front in the winter hemisphere associated with an intense circum-polar vortex. The solstice results show evidence for a strong cross-equatorial meridional (Hadley) circulation. Results from both equinox periods show some hemispheric asymmetry with stronger latitudinal gradients in the Northern Hemisphere in both cases, indicating zonal (eastward) winds almost twice as strong in the north as in the south.

The gradient winds associated with the meridional cross-sections shown in Fig. 2 give strong westerly jets (winds blowing from west to east) at solstice in the winter hemisphere at the latitude of the steep thermal gradient with latitude. Peak winds reach over 160 m s^{-1} at roughly 60° N latitude and $p=0.1$ mbar at $L_s=270^\circ$ and 120 m s^{-1} at roughly 60° S latitude and $p=0.1$ mbar at $L_s=90^\circ$. At $L_s=270^\circ$ there are moderate easterly winds throughout the summer (southern) hemisphere. At $L_s=90^\circ$ there are weak winds at mid- and high-latitudes in the summer (northern) hemisphere transitioning to easterlies at low latitudes. At both equinoxes ($L_s=0^\circ$ and 180°) there are westerly jets at about 50° latitude in both hemispheres, with the

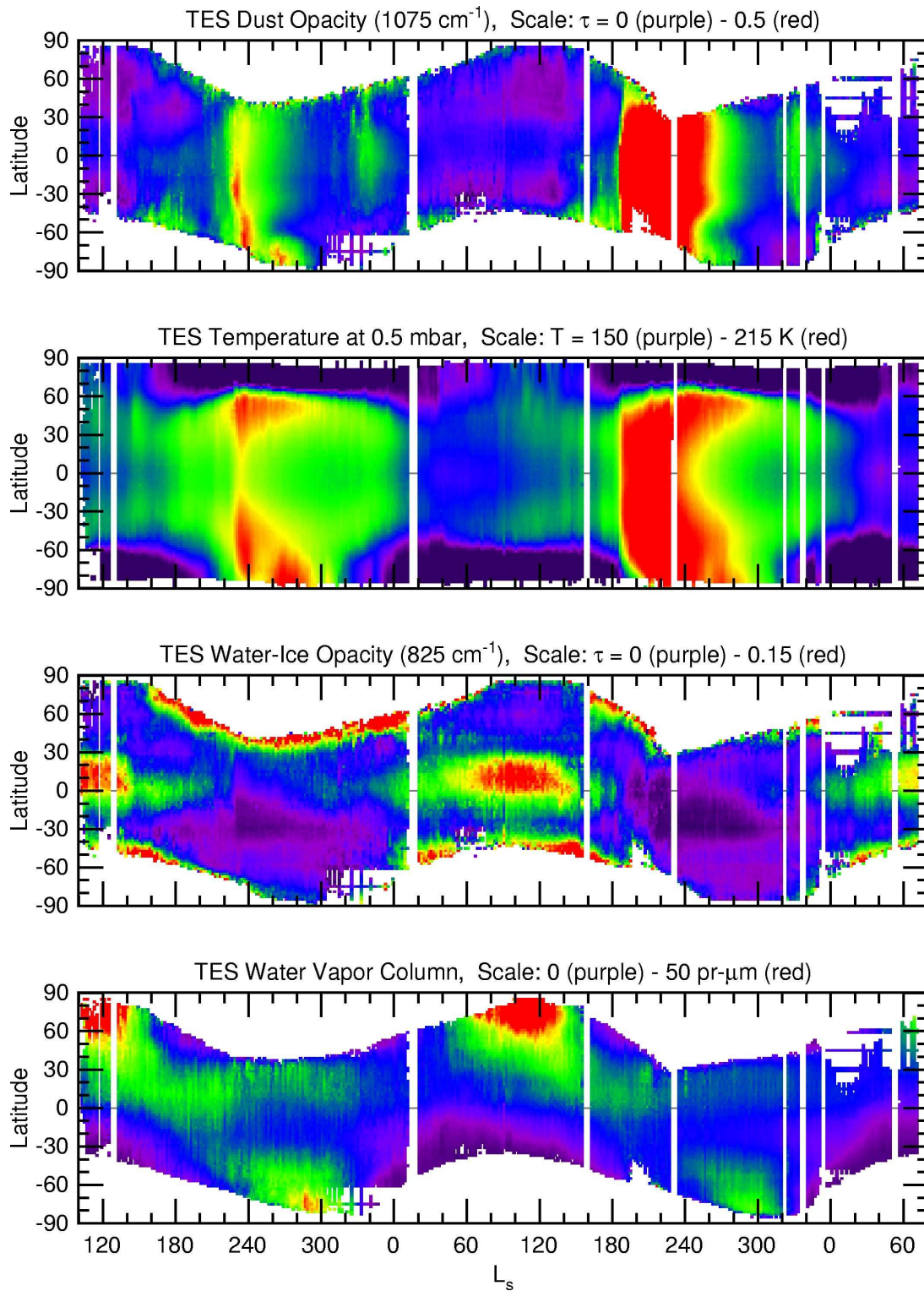


Figure 1. An overview of TES atmospheric dayside (local time ~ 1400 hours) observations is shown as zonal averages as a function of latitude and season (L_s). (top) dust optical depth at 1075 cm^{-1} scaled to an equivalent 6.1 mbar pressure surface, (second) atmospheric temperatures (K) at 0.5 mbar ($\sim 25 \text{ km}$), (third) water-ice optical depth at 825 cm^{-1} , and (bottom) water vapor column abundance in $\text{pr-}\mu\text{m}$. Data gaps (white vertical bands) were caused by spacecraft anomalies and solar conjunction.

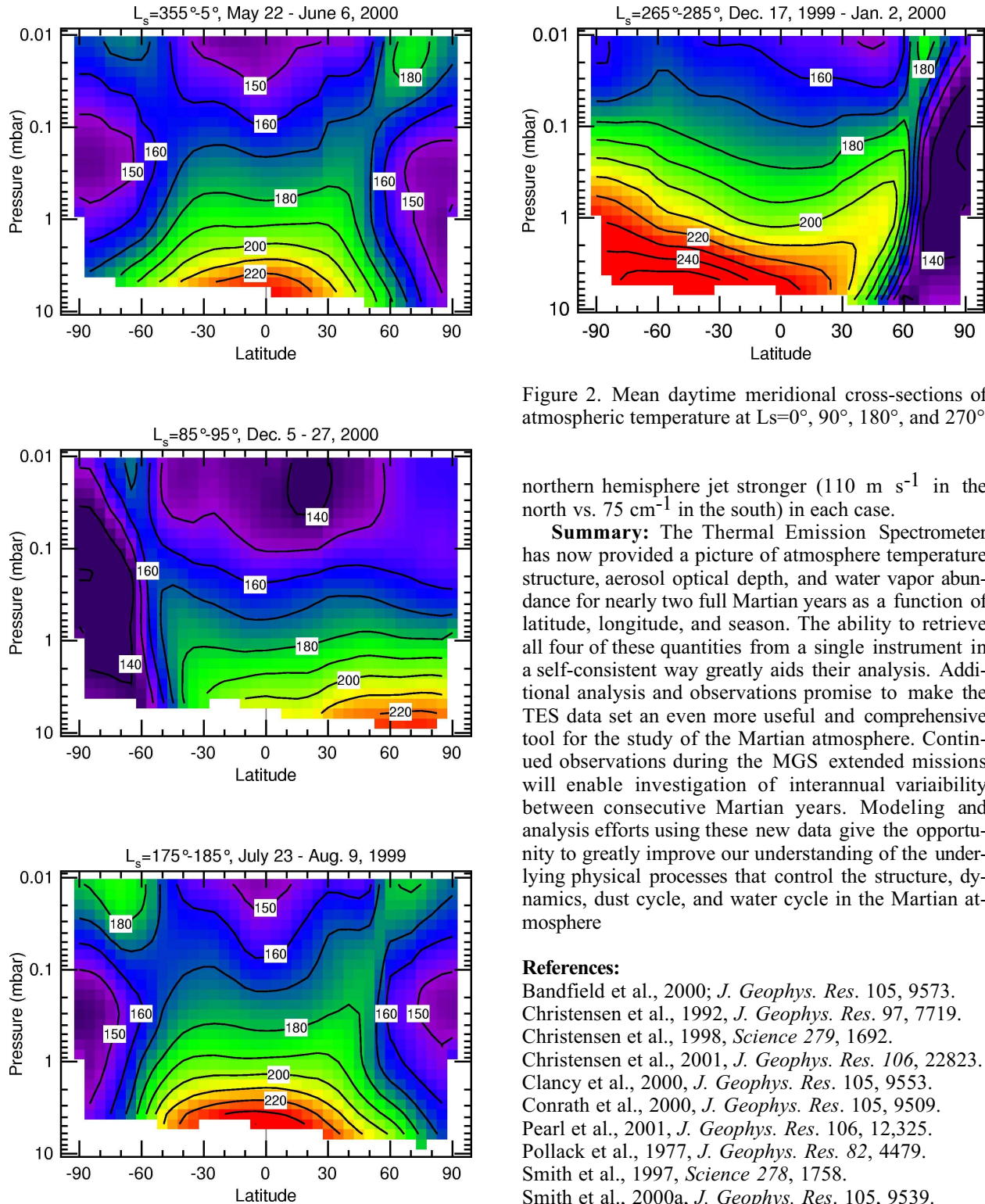


Figure 2. Mean daytime meridional cross-sections of atmospheric temperature at $L_s=0^\circ$, 90° , 180° , and 270°

northern hemisphere jet stronger (110 m s^{-1} in the north vs. 75 m s^{-1} in the south) in each case.

Summary: The Thermal Emission Spectrometer has now provided a picture of atmosphere temperature structure, aerosol optical depth, and water vapor abundance for nearly two full Martian years as a function of latitude, longitude, and season. The ability to retrieve all four of these quantities from a single instrument in a self-consistent way greatly aids their analysis. Additional analysis and observations promise to make the TES data set an even more useful and comprehensive tool for the study of the Martian atmosphere. Continued observations during the MGS extended missions will enable investigation of interannual variability between consecutive Martian years. Modeling and analysis efforts using these new data give the opportunity to greatly improve our understanding of the underlying physical processes that control the structure, dynamics, dust cycle, and water cycle in the Martian atmosphere

References:

Bandfield et al., 2000, *J. Geophys. Res.* 105, 9573.
 Christensen et al., 1992, *J. Geophys. Res.* 97, 7719.
 Christensen et al., 1998, *Science* 279, 1692.
 Christensen et al., 2001, *J. Geophys. Res.* 106, 22823.
 Clancy et al., 2000, *J. Geophys. Res.* 105, 9553.
 Conrath et al., 2000, *J. Geophys. Res.* 105, 9509.
 Pearl et al., 2001, *J. Geophys. Res.* 106, 12,325.
 Pollack et al., 1977, *J. Geophys. Res.* 82, 4479.
 Smith et al., 1997, *Science* 278, 1758.
 Smith et al., 2000a, *J. Geophys. Res.* 105, 9539.
 Smith et al., 2000b, *J. Geophys. Res.* 105, 9589.
 Smith et al., 2001, *J. Geophys. Res.* 106, 23,929.
 Smith et al., 2002, *Icarus* 157, 259.
 Smith 2002. The annual cycle of water vapor on Mars as observed by the Thermal Emission Spectrometer, *J. Geophys. Res.*, in press